Chemical ordering and pressure-induced isostructural and electronic transitions in MoSSe crystal

Achintya Bera [1,*] Anjali Singh [2,*,†] Y. A. Sorb,[3] Ramesh Naidu Jenjeti [4] D. V. S. Muthu,[1] S. Sampath,[4] Chandrabhas Narayana,[3] U. V. Waghmare,[2] and A. K. Sood [1,‡]

[1]*Department of Physics, Indian Institute of Science, Bangalore 560 012, India*
[2]*Theoretical Sciences Unit, Jawaharlal Nehru Centre for Advanced Scientific Research, Jakkur, Bangalore 560 064, India*
[3]*Chemistry and Physics of Materials Unit, Jawaharlal Nehru Centre for Advanced Scientific Research, Jakkur, Bangalore 560 064, India*
[4]*Department of Inorganic and Physical Chemistry, Indian Institute of Science, Bangalore 560 012, India*

Isostructural transitions in layered MX_2 compounds are governed by competing van der Waals (vdW) and Coulomb interactions. While an isostructural transition (at $P \sim 20$ GPa) has been observed before metallization in MoS_2 when subjected to pressure, it is surprisingly missing in layered $MoSe_2$ and $MoTe_2$. Using synchrotron x-ray diffraction and Raman spectroscopic measurements of structural and vibrational properties of layered MoSSe crystals subjected to pressures up to 30 GPa and first-principles density functional theoretical analysis, we demonstrate a layer sliding isostructural transition from its $2H'_c$ structure (space group $P6_3mc$) to a mixed-phase of $2H'_a + 2H'_c$ at $P \sim 10.8$ GPa, marked by discontinuity in lattice parameters, pressure coefficients of Raman modes, and accompanying changes in electronic structure. The origin of the unusually lower transition pressure of MoSSe compared with MoS_2 is shown to be linked to chemical ordering of S and Se atoms on the anionic sublattice, possible because of moderate lattice mismatch between the parent compounds MoS_2 and $MoSe_2$ and large interlayer space in the vdW-bonded structure. Notably, we also report a lower-pressure transition observed at $P \sim 3$ GPa and not reported earlier in the isostructural Mo-based chalcogenides, marked by a discontinuity in the pressure coefficient of the c/a ratio and indirect band gap. The transition observed at $P \sim 10.8$ GPa appears due to the change in the sign of the pressure coefficient of the direct band gap originating from inversion of the lowest-energy conduction bands. Our theoretical analysis shows that the phase transition at $P \sim 18$ GPa marked by sharp changes in pressure coefficients of A_1 Raman modes is associated with the metallization of the $2H'_a$ phase.

I. INTRODUCTION

Transition-metal dichalcogenides (TMDCs) with the chemical formula MX_2 ($X=$ S, Se, and Te) have attracted renewed interest due to the development of their two-dimensional (2D) structural forms exhibiting rich electronic, optical, and chemical properties with potential applications in nanoelectronics [1–3], optoelectronics [4–6], spintronics [7,8], photocatalytic [9–11], energy harvesting [12], and biomedical devices [13], as well as in valleytronics [14]. An interesting aspect of MX_2 compounds is that they occur in several polymorphic forms. For example, bulk MoX_2 can take broadly two types of layered polymorphic forms with distinct coordination of Mo: (i) trigonal prismatic in $2H$-MoX_2 and (ii) octahedral in $1T$-MoX_2. Further variation in the stacking of $1H$-MoX_2 layers results in a variety of polytypes: rhombohedral $3R$, orthorhombic T_d, and monoclinic $1T'$ structures.

Polymorphism holds immense potential in developing 2D electronics [15], particularly in making Ohmic contacts by using a homojunction [16] between the lattice-matched metallic

and semiconducting phases of TMDCs. Raman spectra are useful in the characterization of these polytypic structures [17]. The recent discovery of a type-II Weyl semimetallic state with nontrivial electronic topological signatures [18,19] and the observed superconductivity in the T_d phase of $MoTe_2$ sets TMDCs up as a new platform for the exploration of the quantum spin Hall effect and topological superconductivity [20]. Central to all this is the relative stability of these polymorphs, which can be tuned with temperature, pressure, strain, and alloying.

Alloying is a promising approach to tune the band gaps (and hence the electrical and optical properties) of semiconductors [21,22]. Structural, electronic, and optical properties of alloys can be tuned by varying the concentrations of the constituents [23,24] such that the range of available material properties is much expanded. Semiconductor science and technology have been enormously advanced by alloying different semiconductors to attain continuously tunable electronic structures, for example, Si_xGe_{1-x} for high-mobility transistors [25]. Chemical pressure or strain arises from isoelectronic substitution of ions of different radii in the solid network. The 2D to three-dimensional structural dimensionality evolution is induced by isoelectronic substitution, which is known as chemical pressure, and is suggested to be monitored by the ratio of lattice parameters c/a [26]. The chemical pressure effect in the present study is realized by the isoelectronic

---

substitution of S by Se. With increasing the atomic size of Se, the slab thickness along the c axis increases, and hence, the c/a ratio increases, causing a decrease in the interlayer bonding.

MoX_2 materials consist of X-Mo-X 2D atomic layers stacked along the c direction and bonded together by van der Waals (vdW) interaction. The weak interlayer vdW interaction facilitates the possibility of relative in-plane displacements of adjacent layers [27], making them useful in lubrication applications. Recent high-pressure Raman studies [28–30] on $2H$-MoS$_2$ revealed that there is an onset of lateral slip of the adjacent S-Mo-S layers around $P \sim 20$ GPa, leading to a mixed phase of $2H_c$ (known as H) and $2H_a$ structures with a dominating fraction of the $2H_c$ phase [29] and consequent changes in the pressure coefficients of Raman modes [30]. Completion of the layer sliding transition from a $2H_c$ (semiconductor) to $2H_a$ (metal) structure occurs at $P \sim 40$ GPa [30]. Although the $2H_c$ and $2H_a$ structures of MoS$_2$ share the same crystal symmetry of the $P6_3/mmc$ space group, they are structurally distinct: Mo atoms occupy 2b Wyckoff sites in the $2H_c$ phase, whereas they occupy 2c Wyckoff sites in the $2H_a$ phase. Recent transport and x-ray diffraction experiments show that $2H_a$ MoS$_2$ becomes superconducting below 3 K at 90 GPa and the transition temperature increases to 12 K at 220 GPa [31]. The origin of superconductivity is attributed to the emergence of a new flat pocket in the Fermi surface at high pressure.

The study of isostructural phase transitions under pressure leads to a new way of understanding the mechanisms and the competitive driving forces (vdW and Coulomb) at play [27,32]. The observed $2H_c$ to $2H_a$ transition in MoS$_2$ triggered the search for possible pressure-induced layer sliding isostructural transitions in the similar compounds MoTe$_2$ and MoSe$_2$, before the gap-closing metallic phase transition takes place. However, it was shown [33] experimentally as well as theoretically that MoTe$_2$ ($P6_3/mmc$) does not undergo any structural transition up to pressures of 30 GPa. High-pressure Raman and x-ray diffraction (XRD) studies on MoSe$_2$ ($P6_3/mmc$) [34] confirmed that there is no structural transition up to 36 GPa. While all three Mo-based TMDCs undergo transitions to metallic or semimetallic states, the isostructural transition is known to precede metallization with pressure only in MoS$_2$. The vdW interaction increases with pressure, and it is the strongest for the $2H_a$ phase of MoS$_2$ compared to the $2H_a$ phases of MoSe$_2$ and MoTe$_2$, whereas the Coulombic interaction between Mo and X atoms is stronger in the $2H_c$ phase relative to the $2H_a$ phase for all three Mo-based chalcogenides [27]. Therefore, the reason possibly could be attributed to the enhanced vdW interaction relative to Coulombic interaction between Mo and S favoring Mo atoms on top of each other in the $2H_a$ phase than in the $2H_c$ phase, where Mo atoms occupy sites on top of S atoms [27]. Wider interlayer separation in MoSe$_2$ and MoTe$_2$ due to the larger radius of chalcogen atoms favors Coulomb interactions and hence the $2H_c$ structure [27].

Like the pristine counterparts MoS$_2$ and MoSe$_2$, the mixed chalcogenides with the formula MoS$_{2(1-x)}$Se$_{2x}$ are known to crystallize in the hexagonal structure and are known to be isomorphous over the entire composition range. Density functional theoretical (DFT) calculations have shown that the bond lengths of Mo-S and Mo-Se are shortened compared

to the pristine MoS$_2$ and MoSe$_2$ [35]. Systematic variation of physical, electrical, and electrochemical properties can be realized by tuning the composition of the alloys [36–41]. For example, the photoluminescence of MoS$_{2(1-x)}$Se$_{2x}$ has been shown to continuously vary between 1.87 eV (MoS$_2$) and 1.55 eV (MoSe$_2$) by tuning the composition. Field-effect mobilities of 0.1 and 0.4 cm^2 V^{-1} s^{-1} for the MoS$_{2(1-x)}$Se$_{2x}$ monolayer with $x = 0.15$ and $x = 0.30$ were recently reported [38]. The catalytic efficiency of hydrogen evolution over mixed chalcogenides is higher than that of pristine sulfide and selenide counterparts [38].

In this paper, we present x-ray diffraction and Raman spectroscopic studies on single-crystal MoSSe along with first-principles DFT calculations to investigate structural, vibrational, and electronic properties as a function of pressure. The details of the crystal growth, experimental details, and computational methods are given in the Supplementary Material (Secs. 1 and 2) [42]. We show that the ordered MoSSe structure belongs to the reduced crystallographic symmetry $P6_3mc$ at ambient conditions and an isostructural transition from $2H'_c$ to a mixed $2H'_c + 2H'_a$ phase takes place around 10.8 GPa, as reflected in the lattice parameters as well as in the Raman spectra. In contrast to MoS$_2$ and MoSe$_2$, we observe a low-pressure transition at $P \sim 3$ GPa where pressure coefficients ($d\omega/dP$) of Raman modes undergo a change which correlates with a sharp variation in the c/a ratio observed as a function of pressure. This low-pressure transition at ~ 3 GPa, not reported for MoS$_2$, MoSe$_2$, or MoTe$_2$, is shown, using DFT calculations, to be accompanied by inversion of the lowest-energy conduction bands. Around 18 GPa, a few Raman modes undergo changes in $d\omega/dP$ which are attributed to enhanced semimetallicity associated with the emergence of metallicity in the $2H'_a$ phase.

II. RESULTS AND DISCUSSION

Analysis of the XRD pattern at 0.7 GPa [see Fig. 1(a)] shows that the modeled crystal structure belongs to space group $P6_3mc$ (No. 186), which is a subgroup of $P6_3/mmc$ (No. 194) to which the $2H$-MoS$_2$ structure belongs. Because of the substitution of S by Se, it loses horizontal mirror symmetry $\sigma_h(xy)$, reducing the crystal symmetry from $P6_3/mmc$ to $P6_3mc$ [the unit cell of MoSSe is shown in the inset of Fig. 1(a)]. The (hkl) reflections are marked in Fig. 1. Mo, S, and Se atoms occupy 2b Wyckoff sites, and we name this structure $2H'_c$. We rule out the other possible crystal structures with different chemical ordering with our DFT-based energy calculations as well as Rietveld analysis (Fig. S1 for details).

Upon compression of MoSSe inside a diamond anvil cell (DAC) up to 20.4 GPa, all the XRD lines shift to larger 2θ values (smaller d spacings), as expected from the contraction of the $2H'_c$-MoSSe lattice. The intensity of the (100) line increases with pressure, while the intensities of the (002), (103), and (105) lines decrease. Throughout the pressure range, the relative intensities of intense (100) and (103) lines change gradually; at $P \sim 13.3$ GPa, the intensity of the (100) line becomes almost equal in intensity, and it reaches nearly double that of the (103) line at ~ 20.4 GPa [Figs. 1(b) and 1(c)]. These observations are possible indications of the presence of another phase around 13.3 GPa. Therefore, Rietveld
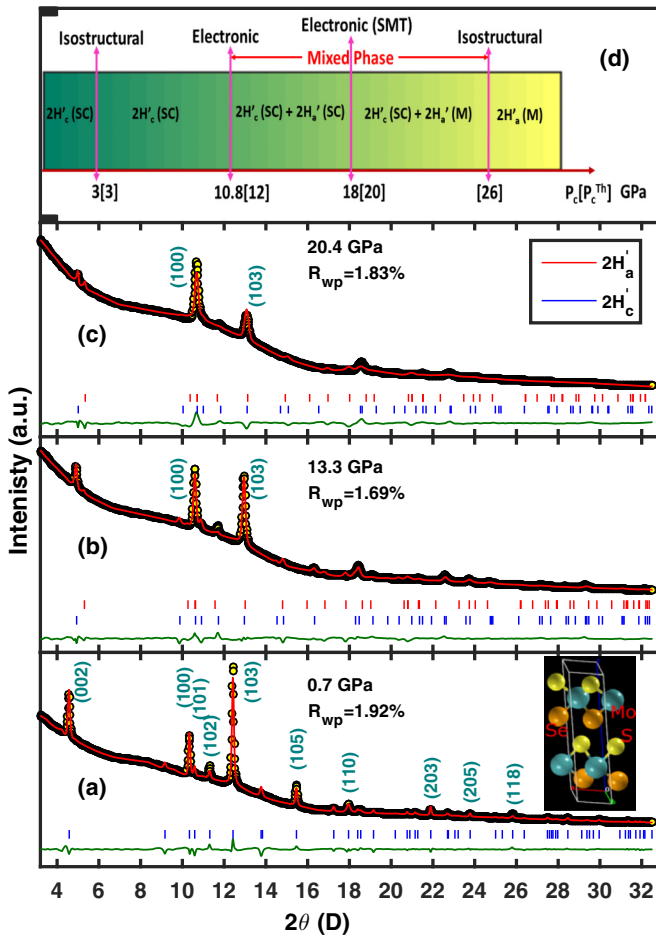
FIG. 1. (a)–(c) XRD patterns at a few elevated pressures; here, a linear scale is shown for intensity (y axis). Rietveld analysis was used to match the patterns to the $P6_3mc$ (No. 186) crystal structure at 0.7 GPa with the GSAS II software package [43]. Here, circles and solid lines represent experimental data and calculated patterns, respectively. The lower curve in dark green is the weighted difference between the observed and calculated patterns. The weighted profile R_{wp} factors are shown. The inset in (a) shows the stacking of atoms in the unit cell. (d) Schematic of phase transitions in MoSSe with pressure.

analysis with fitting to two phases is carried out for the XRD pattern at 13.3 GPa with an additional $2H'_a$ phase, in which Mo atoms in one layer get displaced to sit on top of each other. We follow the two-phase analysis up to the maximum pressure of ∼20.4 GPa [Figs. 1(b) and 1(c)]. The refined atomic coordinates for the $2H'_c$ and mixed phase $2H'_c + 2H'_a$ are listed in the Supplemental Material (Table SI). For the mixed phase of MoS$_2$ [44], the intensities of both the (103) and (105) lines decrease with pressure, similar to our observations for MoSSe. Hromadová et al. [44] pointed out that these changes are indicative of a diminishing $2H_c$ phase along with increasing dominance of the $2H_a$ phase. Our conclusion based on XRD analysis about the emergence of a $2H'_a$ phase agrees well with the DFT-based calculations (discussed later).

The lattice parameters exhibit a discontinuity at $P \sim$ 10.8 GPa with the emergence of the $2H'_a$ phase, marking in-plane expansion and a drop in parameter c [see Fig. 2(a)] at
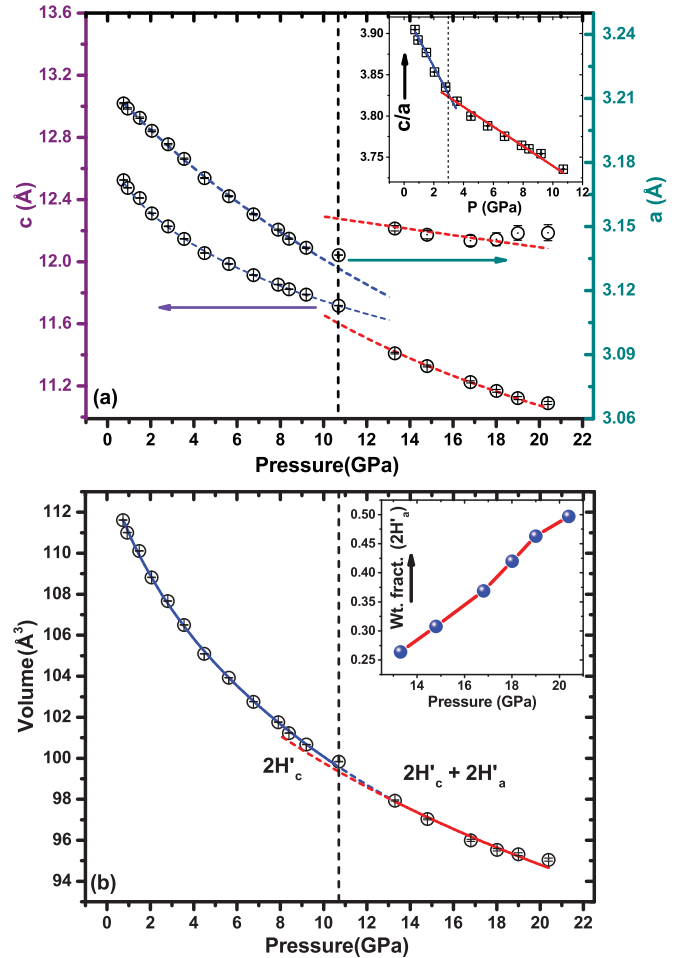

FIG. 2. (a) Variation in lattice parameters with pressure. Here, horizontal arrows point to the corresponding vertical axis. The inset shows pressure variations of the c/a ratio. The curves fitting the P-V data using the third-order BM equation are shown by solid lines in (b). The inset in (b) shows the variations of the weight fraction of the $2H'_a$ phase with pressure. The vertical dashed lines are a guide to the eye. Error bars are less than the size of symbols marking data points.

this transition with the onset of the mixed phase $2H'_c + 2H'_a$. The inset of Fig. 2(a) shows a distinct change in the slope of c/a at ∼3 GPa. Second, there is a clear volume discontinuity at $P \sim 10.8$ GPa [P-V data are fitted to the third-order Birch-Murnaghan (BM) equation of state, as shown in Fig. 2(b)]. From this, the bulk modulus at ambient pressure B_0 is 31.3 ± 3.9 GPa, with its pressure derivative $B'_0 = 17.4 \pm 2.8$ and the ambient pressure volume V_0 being 113.9 ± 0.3 Å^3. In the high-pressure phase ($2H'_c + 2H'_a$), these are $B_0 = 67.4$ GPa (fixed), $B'_0 = 11.7 \pm 1.7$, and $V_0 = 109.26 \pm 0.62$ Å^3. The less anisotropic and stiffer bonding in the mixed phase is reflected in the larger value of B_0. The weight fraction of the $2H'_a$ phase at 13.3 GPa is ∼0.26, which increases up to ∼0.49 at 20.4 GPa, as shown in the inset of Fig. 2(b). We note that the in-plane lattice mismatch of MoSSe with respect to MoS$_2$ ($a = 3.159$ Å and $c = 12.298$ Å) [29] and MoSe$_2$ ($a = 3.283$ Å and $c = 12.918$ Å) [34,45] is 1.53% and 2.30%, respectively, while the out-of-plane lattice mismatch is 1.85% and 3.03%, respectively. Our finding of planar ordered atomic
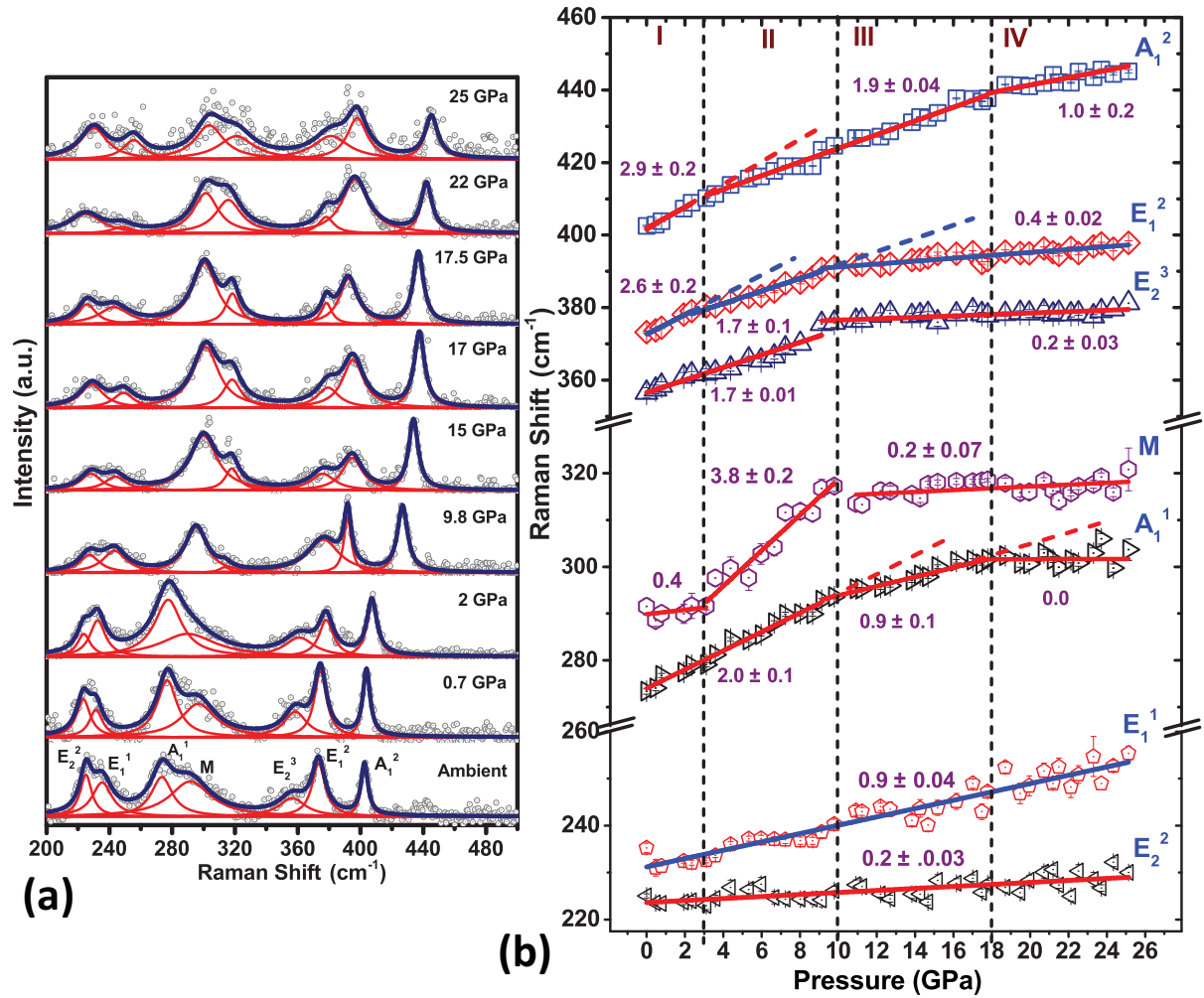
FIG. 3. (a) Evolution of Raman spectra with pressure in the forward cycle. Solid lines are the Lorentzian fits to the experimental data points. (b) Frequencies of the Raman modes as a function of pressure. Solid lines are linear fits [$\omega_p = \omega_0 + (\frac{d\omega}{dP})P$] to the observed frequencies, and the values of slopes are given. Error bars (obtained from the fitting procedure) are also shown. Vertical dashed lines mark the transitions.

arrangements of S and Se in the ternary MoSSe chalcogenide could be attributed to small but nontrivial lattice mismatch between the stoichiometric parent compounds. From our Rietveld analysis and DFT-based calculations, we conclude that three atoms (Mo, S, and Se) occupy the same Wyckoff (2b) positions in the MoSSe structure, whereas Mo atoms occupy 2b Wyckoff sites and S and Se atoms occupy 4f sites [29,34] in MoS$_2$ and MoSe$_2$.

The point group of 2H_c'-MoSSe is C_{6v} with a unit cell containing two formula units, and its phonon modes at the Brillouin zone center (the Γ point) are classified into modes with symmetry labels given by irreducible representations: 3 × $(A_1 + A_2 + B_1 + B_2 + E_1 + E_2)$. Out of these, the A_1 and E_1 modes are both infrared and Raman active, while the E_2 mode is only Raman active. Atomic displacement patterns of each of these modes are shown in Fig. S2 for MoSSe. Raman spectra of MoSSe at a few representative elevated pressures inside the DAC as well as at 0 GPa (marked as ambient) outside the DAC is presented [see Fig. 3(a)]. The origin of mode M at $\omega \sim$ 290 cm^{-1} is discussed in detail later. Throughout the pressure range up to 25 GPa, we do not observe any new modes (see Table I for the assignment of all the observed modes).

Raman modes E_1^2, A_1^2, and M show a change in $d\omega/dP$ at ~3 GPa [Fig. 3(b)], and we suggest that this is linked to the observed changes in the c/a ratio at $P \sim 3$ GPa [inset of Fig. 2(a)]. At $P \sim 10$ GPa, five modes (A_1^1, M, E_2^3, E_1^2, A_1^2) exhibit changes in $d\omega/dP$. The observed changes in $d\omega/dP$ of the Raman modes correlate with the observed volume discontinuity around ~10.8 GPa [Fig. 2(b)], marking the onset of the mixed phase 2H_c' + 2H_a'. The modes A_1^1 and A_1^2 undergo another change in $d\omega/dP$ at $P \sim 18$ GPa. The reduction in the Raman signal-to-noise ratio at higher pressure [see the panel for 25 GPa in Fig. 3(a)] might be associated with the enhanced metallicity discussed later. Like for MoS$_2$ [28,30], the frequency difference plot of the A_1^2 (A_{1g} of MoS$_2$ type) and E_1^2 (E_{2g}^1 of MoS$_2$ type) Raman modes as a function of pressure captures the three transitions at $P \sim 3$, 10, and 18 GPa, as shown in Fig. 4(a). Nayak *et al.* [28] showed for MoS$_2$ that the frequency difference plot between the A_{1g} and E_{2g}^1 modes carries the signature of 2H_c-MoS$_2$ to an intermediate phase and then to the 2H_a phase (metallic phase). In the same spirit, Fig. 4(a) shows the frequency difference plot of the A_1^2 and E_1^2 Raman modes as a function of pressure. It clearly reflects the three different phases: (I) at ~3 GPa because of

TABLE I. Comparison of the observed and calculated frequencies of Raman active modes of MoSSe at 0 and 12 GPa.

Mode	Experiment (cm^{-1})			Theory (cm^{-1})		
	ω at 0 GPa	ω at 12 GPa	$\Delta\omega$	ω at 0 GPa	ω at 12 GPa	$\Delta\omega$
E_2^1				29	56	27
E_2^2	223	224	1	198	208	10
E_1^1	230	242	12	200	214	14
A_1^1	272	292	20	284	307	23
E_2^3	355	372	17	335	355	20
E_1^2	370	390	20	336	358	22
A_1^2	402	423	21	421	446	25
2LA(K) or 2LA(M)	290	310	20	294	315	21

the observed changes in the c/a ratio; (II) at ~10 GPa, as the Mo atoms are getting displaced from the 2b site to the 2a site (mixed $2H_c' + 2H_a'$ phases); and (III) around ~18 GPa because of pressure-induced metallicity of the $2H_a'$ phase (discussed later). On bulk MoS$_2$, Chi *et al.* [30] also observed the changes in slope for the frequency difference plot between the A_{1g}

FIG. 4. (a) The frequency difference plot of the A_1^2 (A_{1g} of MoS$_2$ type) and E_1^2 (E_{2g}^1 of MoS$_2$ type) modes. (b) Calculated frequency difference plot for the A_1^2 and E_1^2 Raman modes as a function of pressure.

and E_{2g}^1 modes around ~20 GPa and attributed them to the displacements of Mo atoms from the 2b Wyckoff site to the 2c Wyckoff site, leading to the layer sliding isostructural transition. For MoS$_2$, a similar split-off feature of the E_{2g}^1 mode above ~20 GPa was reported [30], evidencing the onset of the $2H_a$ phase due to layer sliding. Figure 4(b) shows our DFT-calculated frequency difference plot of A_1^2 and E_1^2 Raman modes as a function of pressure, which clearly shows the three different transition regimes, in agreement with the experimental results. The mixed phase coexists from $P \sim$ 10 GPa [28] to 40 GPa for MoS$_2$ [29,30], whereas for MoSSe, it is observed in the range of P from 10.8 GPa (experimental) to 26 GPa (calculated). A similar low-pressure regime for the onset of the mixed phase in MoSSe can be attributed to their comparable interlayer distances (3.06 Å for MoSSe and 3.02 Å for MoS$_2$). Therefore, it is the van der Waals interaction that drives the observed layer sliding transition for MoSSe similar to that in MoS$_2$.

We now present first-principles DFT analysis of the pressure-dependent behavior of MoSSe. We analyzed four of its chemically ordered structural states described with stacking sequences of AbA′BaB′, AbA′B′aB, AbA′A′bA, and AbA′AbA′ [Figs. 5(a) to 5(d)]. Here, a and b label sites of Mo atoms, A and B label sites of S atoms, and A′ and B′ label sites of Se atoms (these are high-symmetry sites of the 2D hexagonal lattice). Our theoretical prediction of $2H_c'$ as the lowest-in-energy structure with the stacking sequence AbA′BaB′ [Fig. 5(a)] is in excellent agreement with experimental XRD analysis [Fig. 1(a)]. The energies of MoSSe with configurations of AbA′B′aB, AaA′A′aA, and AaA′AaA′ ordering are 13, 89, and 80 meV/f.u., respectively, relative to the $2H_c'$ structure. The two layers of $2H_c'$-MoSSe are connected via weak vdW interaction involving S-Se bonds, in contrast to homopolar S-S or Se-Se bonds in MoS$_2$ or MoSe$_2$ [Fig. 5(a)]. We note that the chemical ordering of S and Se atoms in the MoSSe structure was ascertained with the help of combined theoretical and experimental analysis. The details of various structural forms of MoSSe are mentioned in Table SII.

The $2H_a'$ structure of MoSSe is obtained by sliding the top layer of the $2H_c'$ MoSSe structure in the y direction such that the Wyckoff positions of both the Mo atoms are the same [on top; see Fig. 5(e)]. The energy of the $2H_a'$ phase ($P6_3mc$) is 18 meV/f.u. higher than $2H_c'$-MoSSe at $P \sim 0$ GPa. MoSSe with space group $P\bar{3}m1$ is locally stable, whereas its other two structures with space groups $P\bar{6}m2$ and
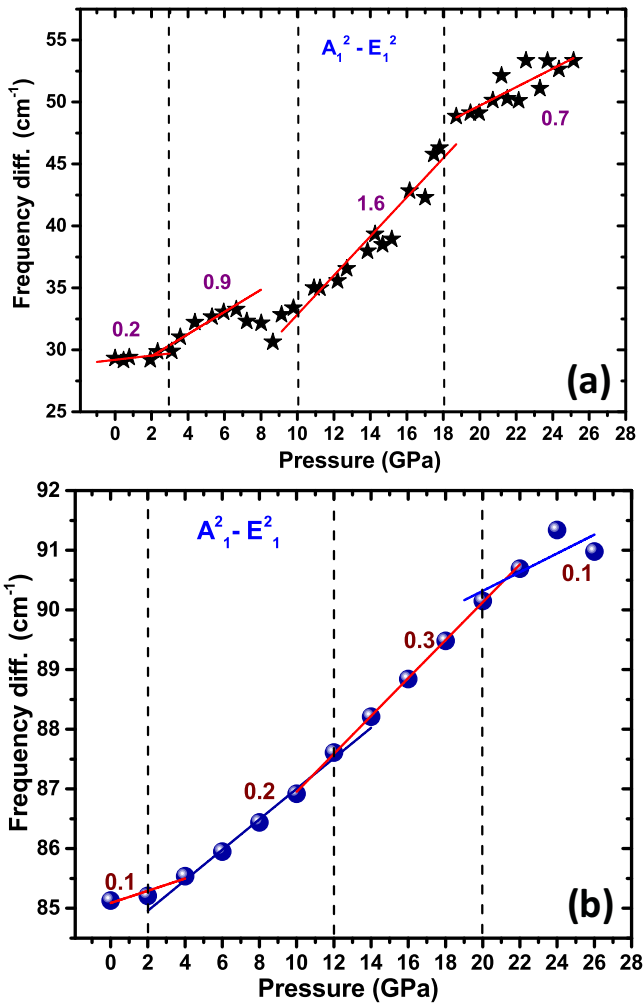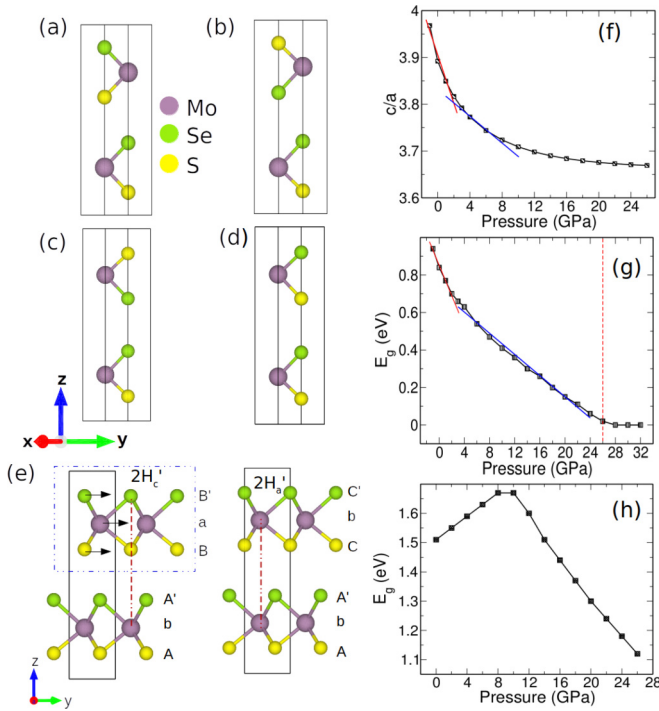
FIG. 5. Layered crystal structures of bulk MoSSe with different stacking sequences: (a) AbA′BaB′ [$2H_c'$; space group (SG): $P6_3mc$], (b) AbA′B′aB (SG: P-3m1), (c) AbA′A′bA (SG: P-6m2), and (d) AbA′AbA′ (SG: $P3m1$). A and B label sites of S atoms, a and b label sites of Mo atoms, and A′ and B′ label sites of Se atoms. (e) Construction of $2H_a'$ (SG: $P6_3mc$) from the $2H_c'$ structure by sliding the top layer in the y direction while keeping the bottom layer fixed (in a given unit cell). (f) Calculated c/a ratio of bulk $2H_c'$ MoSSe. (g) Indirect band gap between bands at Γ and at the midpoint of Γ-K and (h) a direct band gap at the K point of bulk $2H_c'$ MoSSe as a function of pressure. Note that the indirect band gap closes at $P \sim 26$ GPa.

$P3m1$ are locally unstable, as inferred from the lattice instabilities, i.e., imaginary phonon frequencies, in their phonon dispersions (refer to Fig. S3). The calculated structural parameters of the $2H_c'$ phase $a = b = 3.23$ Å, $c = 12.60$ Å (Table SII) are in good agreement with our experiments (Table SI) and exhibit smooth variation as a function of hydrostatic pressure (Fig. S4), signifying the robustness of its structure up to 32 GPa. Our calculations capture the observed low-pressure anomalies in the P coefficients of c/a at $P \sim 3$ GPa [Fig. 5(f)].

The $2H_c'$-MoSSe is an indirect band gap semiconductor with a valence band maximum (VBM) at Γ and a conduction band minimum (CBM) at the K' point (midway along Γ-K) with a gap of 0.84 eV [Fig. S5(a)]. Its phonon dispersion calculated at $P \sim 0$ GPa [Fig. S5(b)] does not exhibit any mode with imaginary frequencies, establishing the local stability of MoSSe in the $2H_c'$ phase. The $2H_c'$ structure of MoSSe remains stable up to 32 GPa, and its indirect band gap undergoes a rapid drop [Fig. 5(g)] up to 3 GPa, followed by a gradual reduction. Interestingly, the direct band gap at the K point increases up to $P \sim 10$ GPa, followed by a monotonous reduction with pressure [Fig. 5(h)]. This originates from the inversion of two of its lowest-energy conduction bands (refer
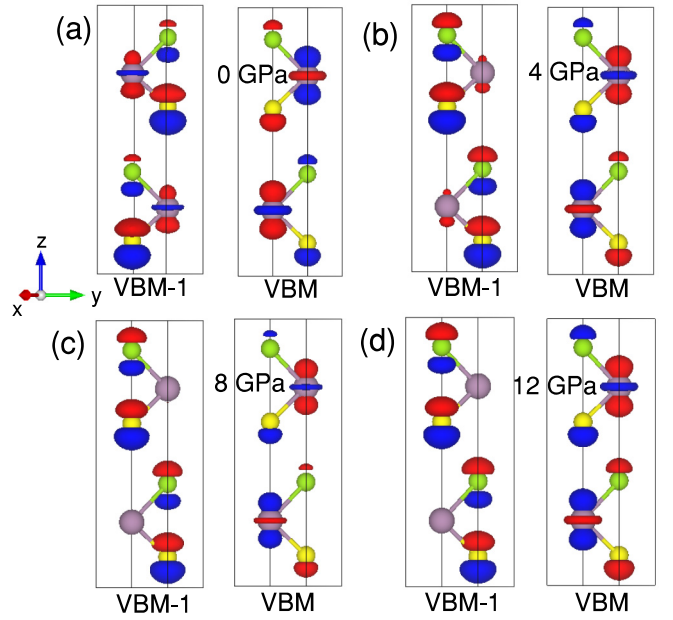

FIG. 6. Isosurfaces of wave functions at VBM-1 and VBM at the Γ point at (a) $P = 0$ GPa, (b) 4 GPa, (c) 8 GPa, and (d) 12 GPa. The isosurface of the VBM does not show any change with pressure, but the VBM-1 isosurface shows significant changes with pressure. The d orbital contribution of Mo atoms decreases with increasing pressure and disappears completely at $P \geqslant 8$ GPa. The wave function at VBM-1 shows mixed symmetry at $P \leqslant 4$ GPa and odd symmetry at $P > 4$ GPa under mirror reflection. Note that the mirror plane is at the Mo atom in the plane of the paper.

to Fig. S6). From the density of states, we find that a small peak (marked by an arrow) appears on top of the VBM which gets further localized at higher pressures (Fig. S7). The origin of this peak is the flat band (VBM-1) at the Γ point (Fig. S8). Furthermore, we visualize the wave function is that of states at the VBM-1 and VBM at the Γ point to understand the nature of this tiny peak. We do not observe any change in the isosurface of the wave function of the VBM, while the wave function of VBM-1 shows interesting changes with pressure. Its contribution from the d orbital of Mo atoms decreases with increasing pressure and disappears completely at $P \geqslant 8$ GPa [Figs. 6(a) and 6(c)] from the isosurface of the wave function of VBM-1. We observe a change in the symmetry of wave functions of VBM-1 at $P \sim 8$ GPa [Figs. 6(b) and 6(c)]: the VBM-1 wave function has mixed symmetry under mirror reflection at $P < 8$ GPa, while it is odd under mirror reflection at $P \geqslant 8$ GPa. At $P \sim 26$ GPa, the indirect gap closes [Fig. 5(g)] with a few states at the Fermi level [Fig. S9(a)] marking the transition of MoSSe to semimetallic states. Therefore, the low-pressure transitions (~ 3 and 10 GPa) are isostructural electronic transitions, and the higher-pressure transition at $P \sim 26$ GPa is an isostructural phase transition from $2H_c'$ to $2H_a'$. Also, the $2H_c'$ structure shows the semiconductor to metal transition at $P \sim 26$ GPa. In fact, it has been shown [46] that the resistivity of bulk MoSSe decreases rapidly in the low-pressure regime of 3 GPa, in agreement with our findings.

Our calculated phonon frequencies agree reasonably well with their observed values (see Table I for a comparison).
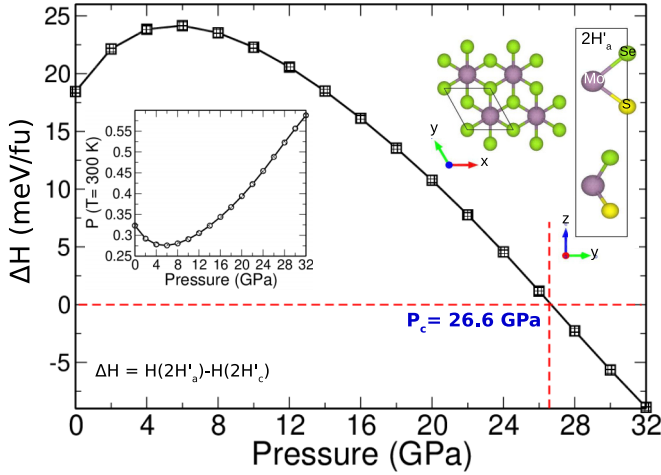
FIG. 7. Difference in enthalpies of $2H_a'$ and $2H_c'$ structures of MoSSe, showing a reversal of their relative stability at 26.6 GPa (at 0 K). The right inset shows the structure of $2H_a'$ in top and side views. Note that in the top view of the $2H_a'$ structure, the Se atom at the center of the hexagon appears from the bottom layer. The probability $\mathbb{P}(T = 300 \text{ K})$ of MoSSe to be in the $2H_a'$ phase as a function of pressure is shown in the left inset.

We identify the mode at $\omega \sim 290$ cm^{-1} [Fig. 3(a)] as a zone boundary phonon, as clearly seen from the two-phonon density of states. We determined phonons of the $2H_c'$ structure with a different stacking sequence (AbA′B′aB) of S-Mo-Se layers [refer to Fig. 5(b)], which belongs to space group $P\text{-}3m1$ (D_{3d}; No. 164), with all atoms in the 2d Wyckoff positions [Fig. 5(b)]. We report all the Raman active modes in Table SIII. The predicted Raman mode at 29 cm^{-1} could not be verified experimentally due to an inaccessible frequency range below 100 cm^{-1} (refer to Table SIII). All the calculated phonon modes as a function of hydrostatic pressure (Fig. S10) exhibit changes in $d\omega/dP$ at $\sim$3, 12, and 20 GPa, consistent with our experimental results [Fig. 3(b)].

The enthalpy difference ΔH $[= H(2H_a') - H(2H_c')]$ between $2H_a'$ and the ambient $2H_c'$ structures becomes negative for $P \geqslant 26.6$ GPa (Fig. 7), consistent with the observed isostructural transition to the $2H_a'$ phase (see Table SII for details). We do not find any phonon instabilities in the $2H_a'$ structure at 0 GPa [Fig. S11(b)] and 28 GPa [Fig. S11(d)], signifying its local structural stability. The $2H_a'$-MoSSe is an indirect band gap semiconductor with a gap of 0.80 eV, having a VBM at the Γ point and a CBM at midpoint along Γ-K [Fig. S11(a)]. The band gap of the $2H_a'$ phase is slightly smaller (by 0.04 eV) than that of the $2H_c'$ phase, and as a result, this phase shows metallic behavior at a lower pressure of $\sim$20 GPa [Fig. S11(c)]. Since at $P > 10$ GPa, both phases ($2H_a'$ and $2H_c'$) coexist, we determined the changes in pressure coefficients of Raman modes of the $2H_c'$ phase at 20 GPa (Fig. S10), which are comparable to the changes observed in experiments at 18 GPa [Fig. 3(b)]. We note that the differences between transition pressures obtained from experiment (3 and 18 GPa) and theory (2 and 20 GPa) are typical and likely due to (I) the error in the DFT estimates of equilibrium lattice constants and (II) the nonhydrostatic stress components possibly occurring in experiments at high pressures. Therefore, we attribute the

observed transition around 18 GPa to the metallization of the $2H_a'$ phase.

Our theoretical estimates of the bulk modulus B_0 of $2H_c'$ and $2H_a'$ structures of MoSSe are 53.1 ± 15.2 and 49.1 ± 12.2 GPa, and their pressure derivatives B_0' are 6.8 ± 2.2 and 6.6 ± 1.6, with ambient volumes V_0 (at $P = 0$ GPa) being 113.8 ± 1.63 and 114.5 ± 1.7 Å^3, respectively. The calculated cell volumes of both the pure phases clearly bear a discontinuity at $P \sim 10$ GPa [Fig. S4(c)]. From our calculations, we find a lower volume for the $2H_a'$ phase than that of the $2H_c'$ phase at P above 10 GPa. We estimated the probability of the occurrence of MoSSe in $2H_a'$ and $2H_c'$ structures as a function of pressure (at $T = 300$ K) using the following equation:

$$\mathbb{P}_{2H_a'}(T = 300 \text{ K}) = \frac{e^{\frac{-\Delta H}{k_B T}}}{1 + e^{\frac{-\Delta H}{k_B T}}},$$

where k_B is the Boltzmann constant. The probability of finding MoSSe in the $2H_a'$ phase increases sharply above 10 GPa and becomes 0.5 at 26 GPa, as shown in the left inset of Fig. 7, confirming the existence of the mixed phase ($2H_c'$ + $2H_a'$) observed in experiments at pressures beyond 10 GPa. Small difference in enthalpies of the two phases supports the feasibility of their coexistence (Fig. 7).

III. CONCLUSIONS

In summary, we have studied structural, vibrational, and electronic properties of bulk $2H_c'$-MoSSe as a function of pressure. An isostructural $2H_a'$ phase is found to coexist with the $2H_c'$ phase above $P \sim 10.8$ GPa, accompanied by changes in the frontier electronic states across the gap. Chemical ordering of S and Se atoms on an anionic lattice of MoSSe arises from a relatively low, but nontrivial, lattice mismatch between the parent compounds and the fact that atoms relax into the interlayer space to accommodate ordering of ions of different sizes. The observed low-pressure (at $P \sim 3$ GPa) transition is marked by the variations in the c/a ratio, and that observed at $P \sim 10.8$ GPa marks the emergence of the mixed $2H_c'$ and $2H_a'$ phase, arising from a sharp change in the electronic structure across the indirect gap. Also, DFT calculations showed a change in the sign of the pressure coefficient of the direct band gap at the K point originating from inversion of the lowest-energy conduction bands. Pressure-induced metallicity of the $2H_a'$ phase is responsible for the transition observed at high pressure ($P \sim 18$ GPa). Our studies will stimulate further high-pressure resistivity measurements to probe the aforementioned electronic signatures, including metallicity and possibly pressure-induced superconductivity, in the $2H_a'$ phase, similar to that observed in the semiconducting $2H$ polymorph of MoS$_2$.

[1] R. S. Sundaram, M. Engel, A. Lombardo, R. Krupke, A. C. Ferrari, P. Avouris, and M. Steiner, Nano Lett. **13**, 1416 (2010).

[2] H. Liu, A. T. Neal, and P. D. Ye, ACS Nano **6**, 8563 (2012).

[3] Y. Cai, G. Zhang, and Y.-W. Zhang, J. Am. Chem. Soc. **136**, 6269 (2014).

[4] D. Voiry, M. Salehi, R. Silva, T. Fujita, M. Chen, T. Asefa, V. B. Shenoy, G. Eda, and M. Chhowalla, Nano Lett. **13**, 6222 (2013).

[5] Z. Yin, H. Li, H. Li, L. Jiang, Y. Shi, Y. Sun, G. Lu, Q. Zhang, X. Chen, and H. Zhang, ACS Nano **6**, 74 (2012).

[6] M. Bernardi, M. Palummo, and J. C. Grossman, Nano Lett. **13**, 3664 (2013).

[7] R. Suzuki, M. Sakano, Y. J. Zhang, R. Akashi, D. Morikawa, A. Harasawa, K. Yaji, K. Kuroda, K. Miyamoto, T. Okuda, K. Ishizaka, R. Arita, and Y. Iwasa, Nat. Nanotechnol. **9**, 611 (2014).

[8] K. F. Mak, K. He, J. Shan, and T. F. Heinz, Nat. Nanotechnol. **7**, 494 (2012).

[9] G. Li, D. Zhang, Q. Qiao, Y. Yu, D. Peterson, A. Zafar, R. Kumar, S. Curtarolo, F. Hunte, S. Shannon, Y. Zhu, W. Yang, and L. Cao, J. Am. Chem. Soc. **138**, 16632 (2016).

[10] Y. Shi, Y. Zhou, D.-R. Yang, W.-X. Xu, C. Wang, F.-B. Wang, J.-J. Xu, X.-H. Xia, and H.-Y. Chen, J. Am. Chem. Soc. **139**, 15479 (2017).

[11] H. Wang, X. Xiao, S. Liu, C.-L. Chiang, X. Kuai, C.-K. Peng, Y.-C. Lin, X. Meng, J. Zhao, J. Choi, Y.-G. Lin, J.-M. Lee, and L. Gao, J. Am. Chem. Soc. **141**, 18578 (2019).

[12] O. S. Lopez, E. A. Llado, V. Koman, A. F. Morral, A. Radenovic, and K. Andras, ACS Nano **8**, 3042 (2014).

[13] S. Karunakaran, S. Pandit, B. Basu, and M. De, J. Am. Chem. Soc. **140**, 12634 (2018).

[14] D. Xiao, G.-B. Liu, W. Feng, X. Xu, and W. Yao, Phys. Rev. Lett. **108**, 196802 (2012).

[15] A. K. Geim and I. V. Grigorieva, Nature (London) **499**, 419 (2013).

[16] R. Kappera, D. Voiry, S. E. Yalcin, W. Jen, M. Acerce, S. Torrel, B. Branch, S. Lei, W. Chen, S. Najmaei, J. Lou, P. M. Ajayan, G. Gupta, A. D. Mohite, and M. Chhowalla, APL Mater. **2**, 092516 (2014).

[17] J.-U. Lee, K. Kim, S. Han, G. H. Ryu, Z. Lee, and H. Cheong, ACS Nano **10**, 1948 (2016).

[18] A. A. Soluyanov, D. Gresch, Z. Wang, Q. S. Wu, M. Troyer, X. Dai, and B. A. Bernevig, Nature (London) **527**, 495 (2015).

[19] H. Weng, C. Fang, Z. Fang, B. A. Bernevig, and X. Dai, Phys. Rev. X **5**, 011029 (2015).

[20] P. Hosur, X. Dai, Z. Fang, and X. L. Qi, Phys. Rev. B **90**, 045130 (2014).

[21] A. Y. Zakharov, Semiconductors **49**, 843 (2015).

[22] A. Lavakumar, *Concepts in Physical Metallurgy* (Morgan and Claypool Publishers, 2017), pp. 6-1–6-6, Chap. 6.

[23] S. H. Wei and A. Zunger, J. Appl. Phys. **78**, 3846 (1995).

[24] S. H. Wei, S. B. Zhang, and A. Zunger, J. Appl. Phys. **87**, 1304 (2000).

[25] J. J. Zhang, K. Shimizu, and J. Hanna, J. Non-Cryst. Solids **299–302**, 163 (2002).

[26] J. Ebad-Allah, J. F. Afonso, M. Krottenmüller, J. Hu, Y. L. Zhu, Z. Q. Mao, J. Kuneš, and C. A. Kuntscher, Phys. Rev. B **99**, 125154 (2019).

[27] X. Fan, D. J. Singh, Q. Jiang, and W. T. Zheng, Phys. Chem. Chem. Phys. **18**, 12080 (2016).

[28] A. P. Nayak, S. Bhattacharyya, J. Zhu, J. Liu, X. Wu, T. Pandey, C. Jin, A. K. Singh, D. Akinwande, and J. F. Lin, Nat. Commun. **5**, 3731 (2014).

[29] N. Bandaru, R. S. Kumar, D. Sneed, O. Tschauner, J. Baker, D. Antonio, S. N. Luo, T. Hartmann, Y. Zhao, and R. Venkat, J. Phys. Chem. C **118**, 3230 (2014).

[30] Z. H. Chi, X. M. Zhao, H. Zhang, A. F. Goncharov, S. S. Lobanov, T. Kagayama, M. Sakata, and X. J. Chen, Phys. Rev. Lett. **113**, 036802 (2014).

[31] Z. Chi, X. Chen, F. Yen, F. Peng, Y. Zhou, J. Zhu, Y. Zhang, X. Liu, C. Lin, S. Chu, Y. Li, J. Zhao, T. Kagayama, Y. Ma, and Z. Yang, Phys. Rev. Lett. **120**, 037002 (2018).

[32] M. Riflikova, R. Martonak, and E. Tosatti, Phys. Rev. B **90**, 035108 (2014).

[33] A. Bera, A. Singh, D. V. S. Muthu, U. V. Waghmare, and A. K. Sood, J. Phys.: Condens. Matter **29**, 105403 (2017).

[34] Z. Zhao, H. Zhang, H. Yuan, S. Wang, Y. Lin, Q. Zeng, G. Xu, Z. Liu, G. K. Solanki, K. D. Patel, Y. Cui, H. Y. Hwang, and W. L. Mao, Nat. Commun. **6**, 7312 (2015).

[35] B. Rajbanshi, S. Sarkar, and P. Sarkar, Phys. Chem. Chem. Phys. **17**, 26166 (2015).

[36] Y. Gong, Z. Liu, A. R. Lupini, G. Shi, J. Lin, S. Najmaei, Z. Lin, A. L. Elías, A. Berkdemir, G. You, H. Terrones, M. Terrones, R. Vajtai, S. T. Pantelides, S. J. Pennycook, J. Lou, W. Zhou, and P. M. Ajayan, Nano Lett. **14**, 442 (2014).

[37] S. Tongay, D. Narang, J. Kang, W. Fan, C. Ko, A. Luce, D. Wang, J. Suh, K. Patel, V. Pathak, J. Li, and J. Wu, Appl. Phys. Lett. **104**, 012101 (2014).

[38] V. Kiran, D. Mukherjee, R. N. Jenjeti, and S. Sampath, Nanoscale **6**, 12856 (2014).

[39] A. Sellam, R. N. Jenjeti, and S. Sampath, J. Phys. Chem. C **122**, 14186 (2018).

[40] H. Li, X. Duan, X. Wu, X. Zhuang, H. Zhou, Q. Zhang, X. Zhu, W. Hu, P. Ren, P. Guo, L. Ma, X. Fan, X. Wang, J. Xu, A. Pan, and X. Duan, J. Am. Chem. Soc. **136**, 3756 (2014).

[41] H. Li, Q. Zhang, X. Duan, X. Wu, X. Fan, X. Zhu, X. Zhuang, W. Hu, H. Zhou, A. Pan, and X. Duan, J. Am. Chem. Soc. **137**, 5284 (2015).

[42] See Supplemental Material at http://link.aps.org/supplemental/10.1103/PhysRevB.102.014103 for experimental details and computational methods, atomic displacements and frequencies of phonons, experimental and calculated lattice parameters, electronic and phonon dispersions for parent and high-pressure phases. It includes a CIF file for the MoSSe crystal structure. It contains the following references: P. Giannozzi, S. Baroni, N. Bonini, M. Calandra, R. Car, C. Cavazzoni, D. Ceresoli, G. L. Chiarotti, M. Cococcioni, I. Dabo *et al.*, J. Phys.: Condens. Matter **21**, 395502 (2009); J. P. Perdew and A. Zunger, Phys. Rev. B **23**, 5048 (1981); S. Goedecker, M. Teter, and J. Hutter, *ibid.* **54**, 1703 (1996); C. Hartwigsen, S. Goedecker, and J. Hutter, *ibid.* **58**, 3641 (1998); T. Thonhauser, S. Zuluaga, C. A. Arter, K. Berland, E. Schröder, and P. Hyldgaard, Phys. Rev. Lett. **115**, 136402 (2015); T. Thonhauser, V. R. Cooper, S. Li, A. Puzder, P. Hyldgaard, and D. C. Langreth, Phys. Rev. B **76**, 125112 (2007); K. Berland, V. R. Cooper, K. Lee, E. Schröder, T. Thonhauser, P. Hyldgaard, and B. I. Lundqvist, Rep. Prog. Phys. **78**, 066501 (2015); D. C. Langreth, B. I. Lundqvist, S. D. Chakarova-Käck, V. R. Cooper, M. Dion, P. Hyldgaard, A. Kelkkanen, J. Kleis *et al.*, J. Phys.: Condens. Matter **21**, 084203 (2009); R. Sabatini, E. Kuçukbenli, B. Kolb, T. Thonhauser,

and S. de Gironcoli, *ibid.* **24**, 424209 (2012); S. Baroni, S. De Gironcoli, A. Dal Corso, and P. Giannozzi, Rev. Mod. Phys. **73**, 515 (2001); S. Adachi, *GaAs and Related Materials* (World Scientific, Singapore, 1994), p. 969.

[43] B. H. Toby and R. B. Von Dreele, J. Appl. Crystallogr. **46**, 544 (2013).

[44] L. Hromadová, R. Martoňák, and E. Tosatti, Phys. Rev. B **87**, 144105 (2013).

[45] P. B. James and M. T. Lavik, Acta Crystallogr. **16**, 1183 (1963).

[46] H. S. Chaki, G. K. Sonalki, A. G. Patel, and S. G. Patel, High Pressure Res. **28**, 133 (2008).